Preprints.org

Article

Experimental Investigation on Fatigue Crack Propagation in Surface Hardened Layer of High-Speed Train Axles

Chun Gao , Zhengwei Yu , Yuanyuan Zhang , Tao Fan , Bo Zhang , Huajian Song , Hang Su [*]

Article

Experimental Investigation on Fatigue Crack Propagation in Surface Hardened Layer of High-Speed Train Axles

Chun Gao [1,2], Zhengwei Yu [3], Yuanyuan Zhang [1], Tao Fan [4], Bo Zhang [5], Huajian Song [6] and Hang Su [7,*]

[1] School of Civil Engineering, Harbin University, Harbin 150086, China

[2] Heilongjiang Province Key Laboratory of Underground Engineering Technology, Harbin University, Harbin 150086, China

[3] College of Science, Heilongjiang University of Science and Technology, Harbin 150020, China

[4] Heilongjiang Zhongbei Post and Telecommunications Construction and Development Company, Harbin 150036, China

[5] Zhongte (Shenzhen) Intelligent Co., Ltd, Shenzhen 518000, China

[6] School of Automation and Electrical Engineering, Linyi University, Linyi 276000, China

[7] Department of Civil Engineering, University of California, Los Angeles, CA 90095, USA

* Correspondence: hangsu2018@g.ucla.edu

Abstract

This paper presents an experimental investigation on fatigue crack propagation in the surface hardened layer of high-speed train axles made of S38C steel. Three-point bending specimens were extracted from CRH2 EMU axles, with the hardened surface layer (0–2 mm depth) and core matrix (beyond 6 mm) characterized via microstructure and microhardness analysis. Fatigue tests were conducted using a PLG100 machine, monitoring crack growth under stress ratio $R = 0.1$. Results show that the hardened layer exhibits lower fatigue crack growth rate (da/dN) than the transition layer (2–6 mm) and core matrix. The da/dN-ΔK relationships were fitted following Paris Law, revealing the hardened layer's higher resistance to crack propagation, attributed to its tempered martensite microstructure. This study provides insights into how gradient microstructures affect fatigue behavior in axle materials.

Keywords: fatigue crack propagation; three-point bending; crack measurement; fractography; high-speed train axle; surface hardening

1. Introduction

High-speed railways have emerged as a cornerstone of modern sustainable transportation, with over 80,000 km of high-speed tracks operational worldwide by 2025 [1,2]. The reliability of key components like axles is critical, as fatigue failure in their surface-hardened layers poses significant safety risks [3–5]. Axles endure cyclic loading exceeding 10^8 cycles during their service life, necessitating investigations into very high cycle fatigue (VHCF) behavior which is defined as fatigue failure beyond 10^7 cycles [6–14]. Traditional studies [15–21] on fatigue crack propagation (FCP) often focus on low-to-high cycle regimes, leaving a knowledge gap in VHCF mechanisms for gradient microstructures [22–25] in hardened layers.

The surface-hardened layer of axles [26–31], typically composed of tempered martensite (0–2 mm depth), transitions to pearlite-ferrite mixtures in the core region [23,32–35]. This gradient microstructure, induced by induction heating, enhances wear [36–38] and fatigue resistance [39–43]. However, in VHCF regimes, crack initiation from sub-surface inclusions or microstructural defects

becomes prevalent, differing from high-cycle fatigue (HCF) failure modes [44–47]. For instance, Pan et al. [48,49] observed that in titanium alloys, VHCF cracks initiate from nanograin formations near inclusion-matrix interfaces, while core materials exhibit faster crack growth rates. Such findings highlight the need to link microstructural gradients with VHCF performance in axle steels.

Additive manufacturing (AM), particularly laser-based powder bed fusion, has revolutionized material design by enabling tailored gradient microstructures [50–56]. Unlike conventional induction hardening, AM allows precise control over hardness [57,58] and phase distributions, potentially optimizing fatigue resistance [59]. In axle steels, AM could mitigate stress concentrations by integrating gradient layers with tailored hardness profiles, though its application in large-scale components like axles remains underexplored.

Current research on axle fatigue primarily relies on conventional testing methods, overlooking the synergistic effects of microstructural gradients and VHCF. Studies by Zhang et al. [23] revealed that in S38C steel, the hardened layer's tempered martensite delays crack propagation, but the transition layer (2–6 mm) exhibits scatter in fatigue crack growth rate (da/dN) due to mixed microstructures. Meanwhile, AM-induced gradients in AlSi10Mg show reduced da/dN in VHCF, attributed to nanograin formation at crack tips [45]. These insights suggest that combining surface hardening with AM could enhance axle durability, yet experimental data on such hybrid approaches remain scarce.

This study addresses these gaps by investigating FCP in induction-hardened S38C axle steel under VHCF conditions (up to 10^8 cycles). Three-point bending specimens with gradient microstructures (hardened layer, transition layer, core) were tested to characterize da/dN and stress intensity factor range (ΔK) relationships. By integrating findings from VHCF research on gradient materials [23,25,45] and AM's potential for microstructure tailoring [60], this work aims to: (1) establish da/dN-ΔK models for different depth zones; (2) compare fatigue resistance between induction-hardened and conceptually AM-optimized microstructures; (3) provide guidelines for improving axle longevity via microstructure design. The results bridge the gap between conventional surface hardening and emerging AM technologies in VHCF-resistant component design.

2. Materials and Methods

2.1. Specimen Design and Fabrication

The axle involved in this research belongs to the CRH2 EMU series (Japanese type), with its base material being S38C steel, as illustrated in Figure 1. The surface of this axle undergoes induction heating, quenching, and low-temperature tempering (induction heating frequency of 3 kHz, heated to 880–900°C followed by water cooling and tempering at 200°C), resulting in a hardened surface layer while maintaining a normalized structure in the core. The surface layer of the axle consists of tempered martensite with a depth of approximately 2 mm. From 2 mm to around 6 mm beneath the surface, there exists a transition layer characterized by a mixture of quenched-tempered microstructure and pearlite-ferrite phases, with an increasing presence of pearlite and ferrite as the depth increases. Beyond 6 mm from the surface, the microstructure predominantly consists of a pearlite-ferrite mixture, indicating a normalized state. The Vickers microhardness within the first 2 mm of the surface layer is approximately 551 ± 36 HV Beyond 2 mm, the microhardness significantly decreases, reaching around 230 HV at a depth of 6 mm, which is close to the hardness of the core material. Beyond 8 mm, the hardness fluctuates slightly within a narrow range, averaging 200 HV representative of the normalized microstructure of the core.
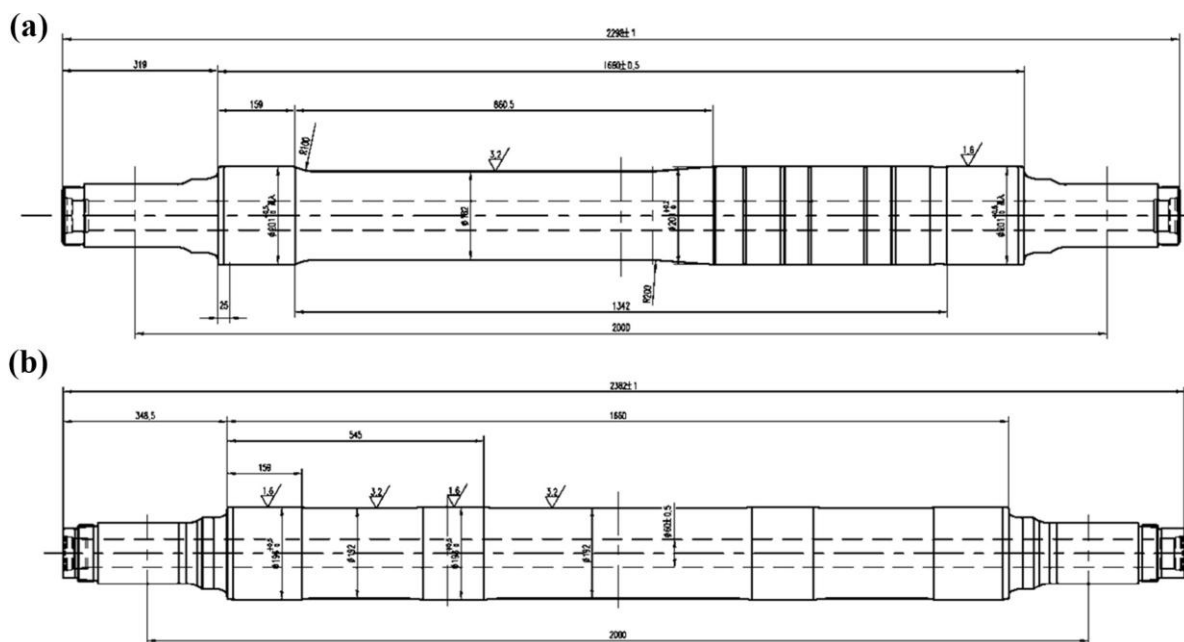
Figure 1. Schematics of (a) high-speed train locomotive axle, (b) high-speed train trailer axle. (unit: mm).

To acquire the fatigue crack growth characteristics of the axle material containing a hardened surface layer, the specimens were designed as three-point bending samples, following the standard specimen dimensions outlined in GB/T4161-2007. The actual dimensions used for the specimens were: 150 mm in length (span of 120 mm), 15 mm in width, and 30 mm in height, as shown in Figure 2a. The tension side of the specimen represents the axle surface, i.e., the hardened surface layer, and a 0.5 mm deep notch was pre-machined at the center of the tension side using CNC wire cutting technology to facilitate crack initiation and growth. Based on the principles of three-point bending beams, the nominal stress on the tensile side surface of the specimen can be calculated as follows:

$$\sigma = \frac{3Px}{wh^2} \tag{1}$$

where σ represents the nominal stress at the notch, P is the applied load, w is the specimen width, h is the specimen height, and x is the half-span length.

Two axle segments were provided, each with a height of 170 mm, extracted from the middle section of the actual trailer axle. Based on the designed specimen shape and dimensions, the cutting scheme was established as shown in Figure 2b. A total of 24 three-point bending specimens were evenly distributed and cut from the surface layer along the circumferential direction of the axle segment. To ensure precision during specimen cutting, the axle's central axis was meticulously measured, and the axle segments were mounted on the cutting machine to ensure that the wire cutting process was perfectly aligned with the axle's axis.
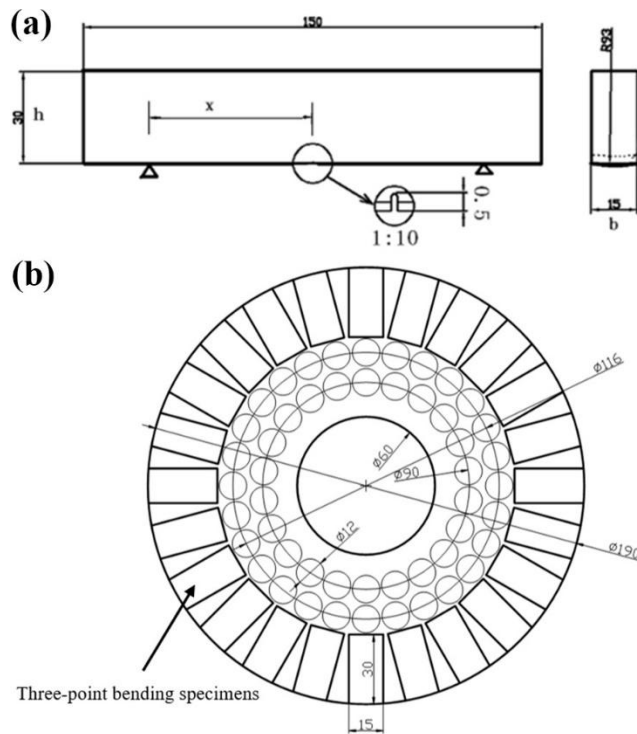
Figure 2. Schematics of (a) three-point bending specimen, (b) axle cross-sectional sampling. (unit: mm).

The front and back surfaces (30 mm × 150 mm) of the extracted three-point bending specimens were ground using a surface grinder, with the surface roughness controlled to R_a = 0.4 μm. The two support points on the surface layer of the specimen (i.e., the support surface or the tensile surface) were also ground to ensure stable support during loading. The middle region of the side surface of the processed specimens was sequentially polished with 400 grit, 800 grit, 1000 grit, 1500 grit, and 2000 grit sandpapers, followed by further polishing with 1.0 μm diamond paste. The actual width and height of the processed and polished specimens were measured by digital calipers. The actual dimensions of the 6 specimens used in this research are listed in Table 1.

Table 1. The actual sizes of the three-point bending specimens.

Specimen Number	Width (mm)	Height (mm)
1	15.60	30.90
3	16.00	31.00
4	16.00	30.70
8	15.98	31.20
17	15.88	30.80
21	15.70	31.00

2.2. Testing Method and Devices

These specimens provide the opportunity to investigate and analyze the fatigue crack growth characteristics of the hardened surface layer of the axle, which exhibits variations in microstructure and mechanical properties across different depths. A PLG100 high-frequency fatigue testing machine, as shown in Figure 3a, was employed to perform three-point bending fatigue loading on the specimens, with a stress ratio R of 0.1. An optical imaging and data acquisition system, as shown in Figure 3b, was used to observe the notched region on the side surface of the three-point bending specimens. Once crack initiation occurred, the propagation of the crack was tracked continuously. The fatigue loading was paused at specific intervals to photograph the crack, and then loading was resumed. Subsequently, image processing software was used to measure the crack length corresponding to each loading cycle. By analysis and calculation, the relationships among crack

length, fatigue crack growth rate, and stress intensity factor were established. For the specimens that reached the termination criteria of the experiment, low-temperature brittle fracture was induced, and the fracture surfaces were photographed using a stereomicroscope. Further analysis of the fracture surfaces was conducted with SEM. The stress intensity factor range ΔK for the crack body in the three-point bending specimens can be calculated using the following equation:

$$\Delta K = \Delta \sigma \sqrt{\pi a} \, f\left(\frac{a}{b}\right) \tag{2}$$

$$f\left(\frac{a}{b}\right) = \frac{1}{\sqrt{\pi}} \frac{1.99 - \frac{a}{b}\left(1 - \frac{a}{b}\right)\left(2.15 - 3.93\frac{a}{b} + 2.7\left(\frac{a}{b}\right)^2\right)}{\left(1 + 2\frac{a}{b}\right)\left(1 - \frac{a}{b}\right)^{\frac{3}{2}}} \tag{3}$$

where $\Delta \sigma$ is the nominal stress amplitude corresponding to the applied load, a is the crack length, and b is the specimen height.

The fatigue crack growth rate (da/dN) is calculated using the differential method, expressed as follows:

$$da/dN = \frac{The\ crack\ length\ at\ the\ Nth\ cycle - The\ crack\ length\ at\ the\ Mth\ cycle}{N - M} \tag{4}$$
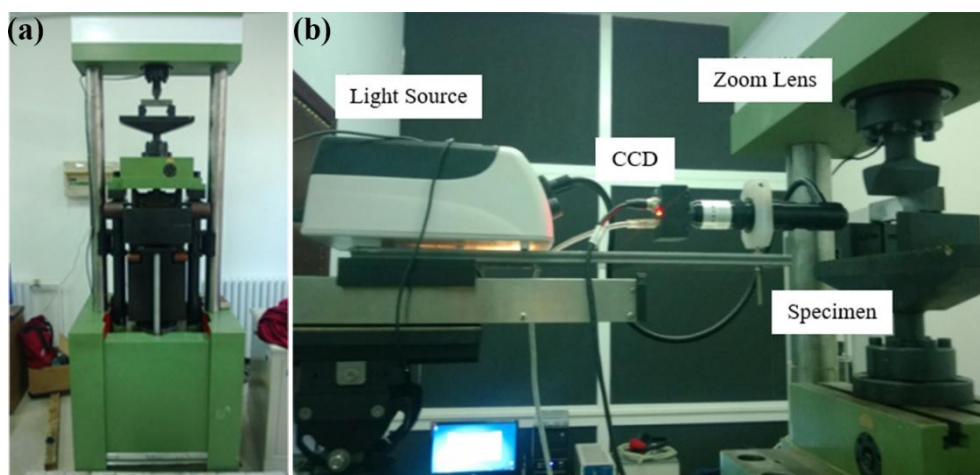

Figure 3. Fatigue testing system: (a) PLG100 high-frequency fatigue testing machine (frequency range: 80–250 Hz, maximum loading: ±50 kN), (b) imaging and data acquisition system.

The testing was conducted in several steps. After installing the specimen and the optical observation equipment, the fatigue experiment is initiated. Once a fatigue crack appears and propagates to a certain length, the fatigue loading is paused to photograph the crack. If the crack does not propagate after 10^6 cycles at a given length, the applied stress is increased (minimum 5 MPa, maximum 20 MPa), and observations are continued. The process is repeated until the crack length exceeds 13 mm or the fatigue testing machine fails to maintain vibration. Then, the captured images are stitched together using image processing software. The crack length on the surface is measured using specialized software. After completing the fatigue experiment, the specimens are rapidly fractured in a liquid nitrogen environment. The fracture surfaces are photographed using a stereomicroscope. Five evenly spaced measurement points are selected perpendicular to the crack propagation direction to measure the distance from the specimen surface to the crack trace at different cycle numbers. The crack growth length is obtained through this measurement, and the crack length observed on the surface is corrected using linear interpolation, as illustrated in Figure 4. Finally, the

relationships among crack length, fatigue crack growth rate, and stress intensity factor range are obtained through calculation.
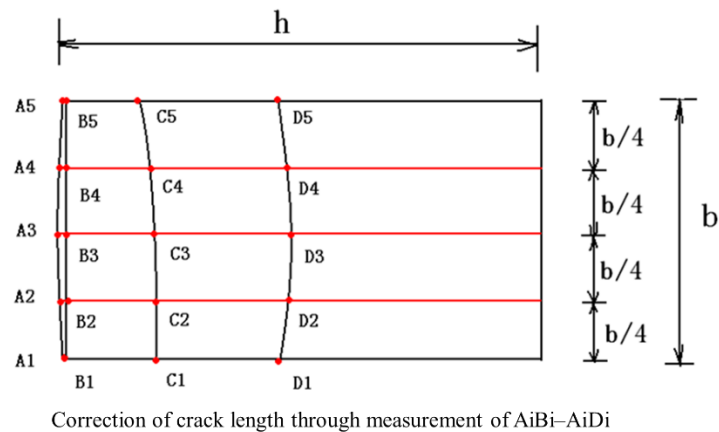

Correction of crack length through measurement of AiBi–AiDi

Figure 4. Schematic of crack measurement.

3. Results

3.1. a–N Data and Fractography

Fatigue crack growth experiments were conducted on the six three-point bending specimens listed in Table 1. For each specimen, the crack length, along with the corresponding applied load and loading cycles, was recorded at various stages of crack propagation after initiation.

Figure 5 displays the results for Specimen 1, including six optical micrographs showing the crack initiation and its progression towards fracture at different stages. Figures 6 presents the observed results of crack growth length versus the number of loading cycles for the 6 specimens, namely the *a–N* data plots. Figure 7 shows the corresponding fractographic observations for the six specimens, each illustrating microstructure and morphology of the fracture surface optically.
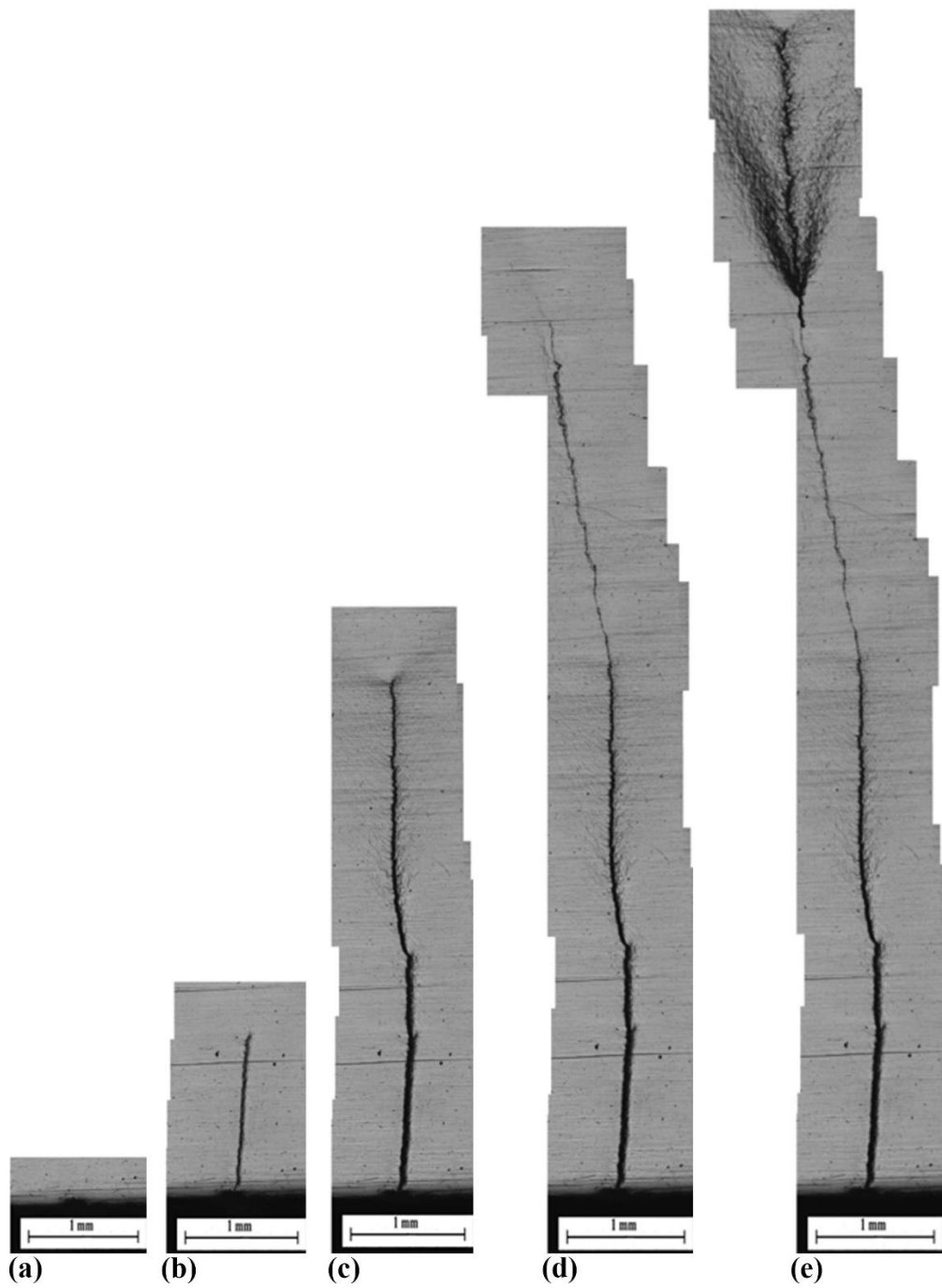
Figure 5. Optical observations of fatigue crack propagation of Specimen 1: (a) original specimen, (b) crack length ~1.4 mm, (c) crack length ~4.6 mm, (d) crack length ~8.2 mm, and (e) crack length ~10.2 mm.
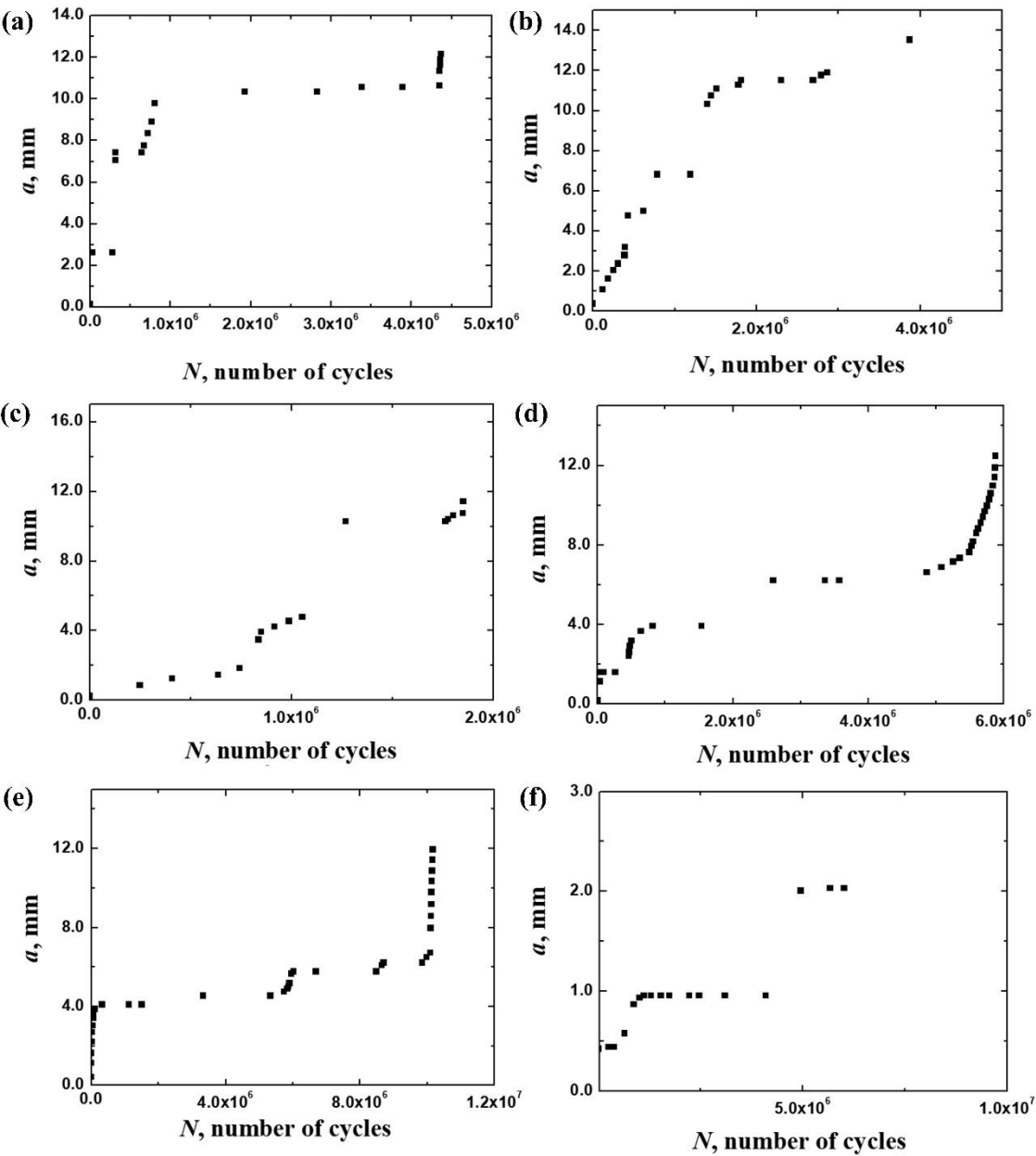
Figure 6. *a–N* data: (a) Specimen 1, (b) Specimen 3, (c) Specimen 4, (d) Specimen 8, (e) Specimen 17, and (f) Specimen 21.
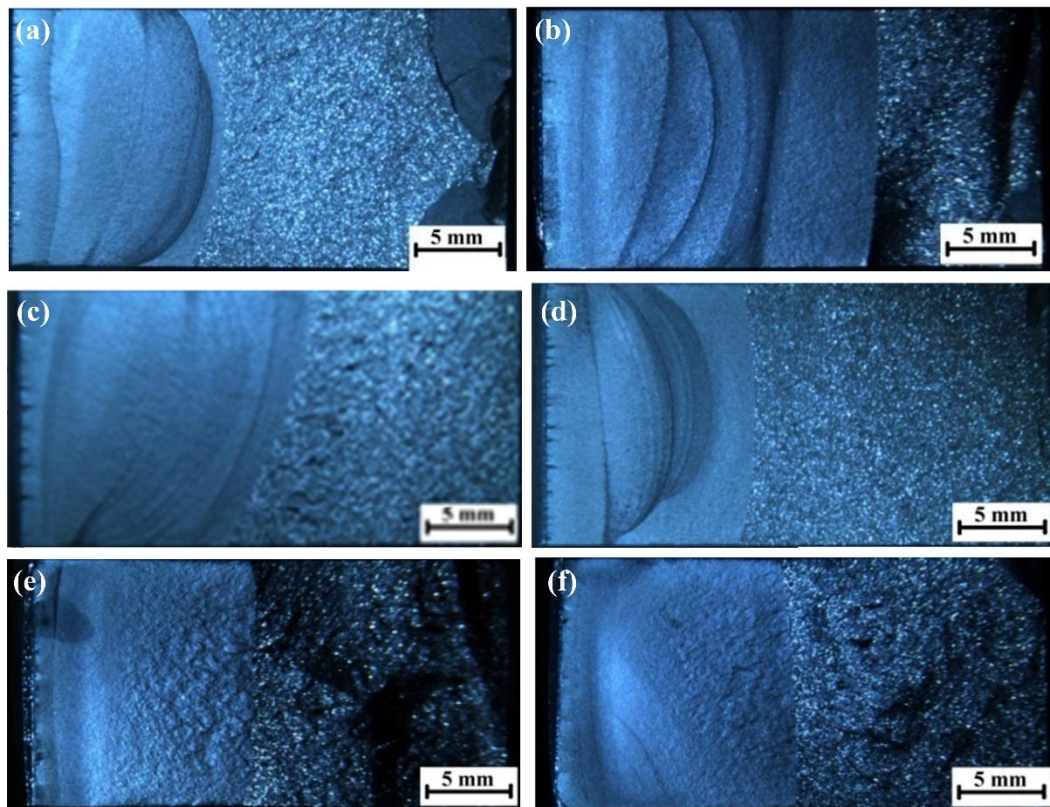
Figure 7. Fractographic observations: (a) Specimen 1, (b) Specimen 3, (c) Specimen 4, (d) Specimen 8, (e) Specimen 17, and (f) Specimen 21.

3.2. da/dN and ΔK Data

The fatigue crack growth experiments yielded the crack growth rate da/dN and the stress intensity factor range ΔK at various stages of crack propagation for each specimen. Due to the gradient variation in the microstructure of the hardened surface layer, da/dN differs at various positions within the hardened layer and the transition layer. Therefore, this research presents experimental results correlating da/dN, ΔK, and the distance of the crack tip from the surface X. Figure 8 illustrates the relationship among da/dN, ΔK, and X for the 6 specimens.
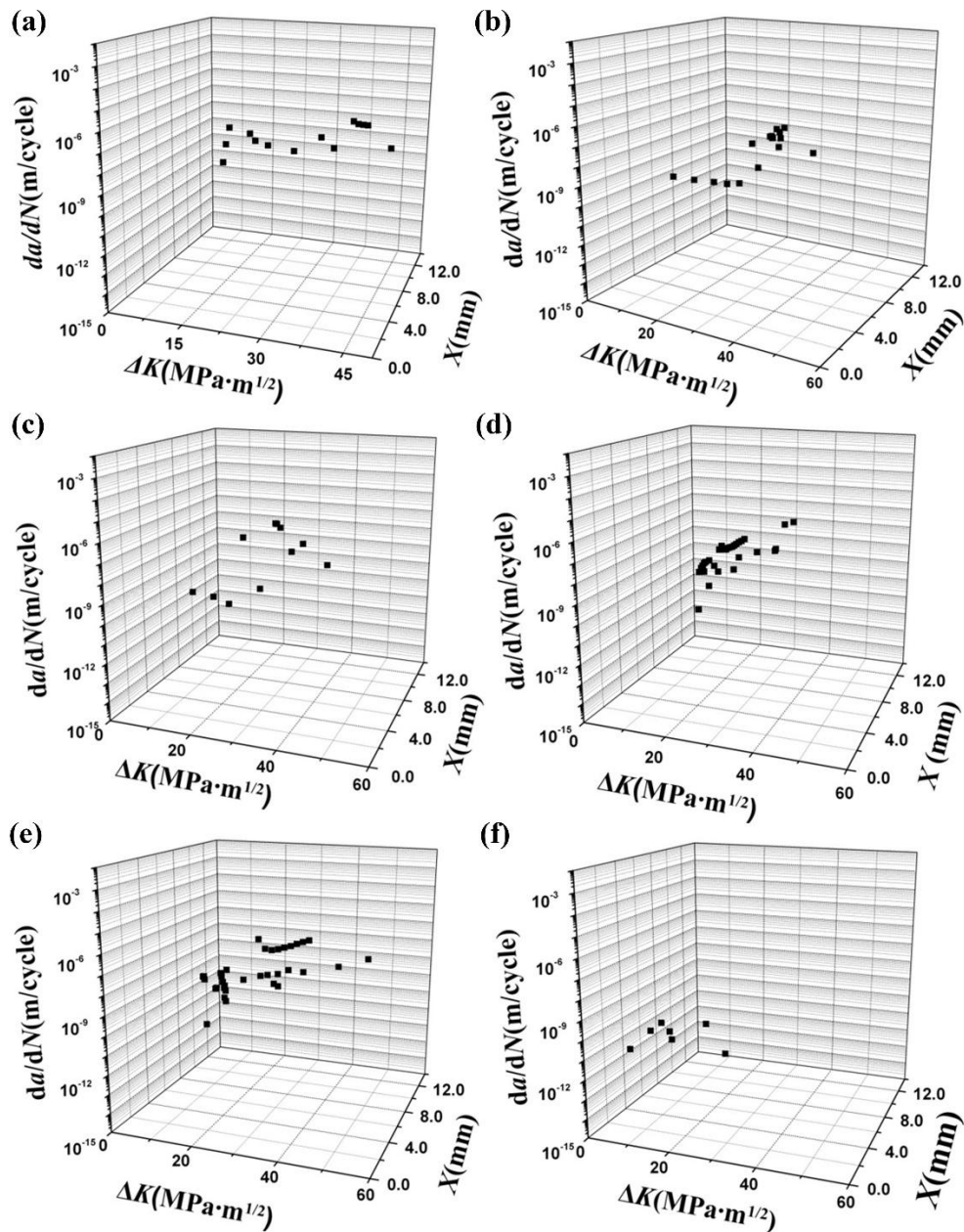
Figure 8. The relationship among d*a*/d*N*, Δ*K*, and *X*: (a) Specimen 1, (b) Specimen 3, (c) Specimen 4, (d) Specimen 8, (e) Specimen 17, and (f) Specimen 21.

4. Discussion

4.1. Summary and Analysis of da/dN and ΔK Data

    The data for the six specimens are consolidated and comprehensively represented in Figure 9. Figure 9a shows the summarized relationship as a d*a*/d*N*–*X*–Δ*K* surface plot and Figure 9b presents the summarized data in a d*a*/d*N*–Δ*K*–*X* plot. From Figure 9, as well as the original data in Figure 8, it is evident that d*a*/d*N* tends to increase with the rise of both Δ*K* and *X*.

(a)   **(b)**

Figure 9. Summary diagrams of d*a*/d*N* and Δ*K* data: (a) d*a*/d*N*–*X*–Δ*K*, and (b) d*a*/d*N*–Δ*K*–*X*.

4.2. da/dN and ΔK in Multiple Depth Ranges

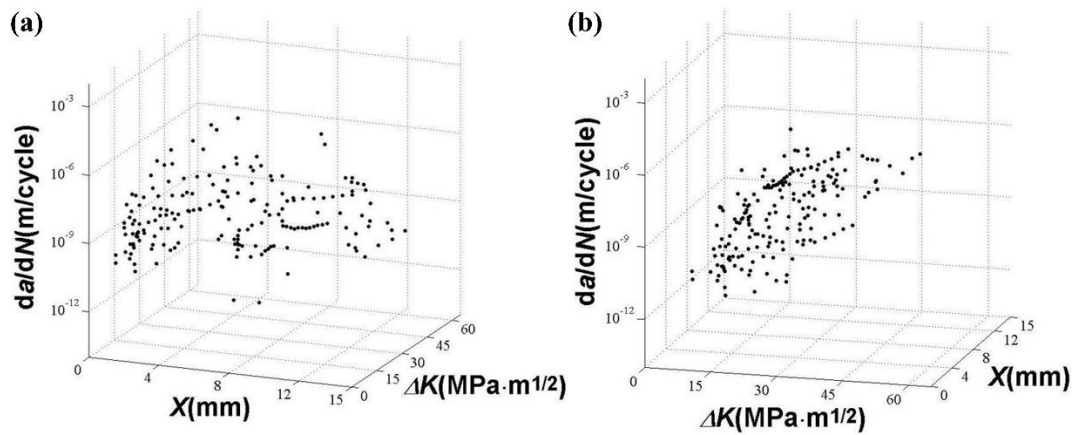Evidently, materials with different microstructures exhibit varying mechanical properties, which, in turn, influence their fatigue crack growth rates. The three-point bending specimens used in the experiment were directly extracted from the actual axle, with the tensile side representing the hardened surface layer of the axle. The surface layer can be divided into three distinct regions based on microstructural characteristics. The region in the depth range of 0–2 mm constitutes the quenched-tempered microstructure of the hardened surface layer. Between 2–6 mm, it's the transition layer, which consists of a mixture of quenched-tempered structures and pearlite-ferrite phases. Beyond 6 mm, it corresponds to the core matrix, characterized by a normalized structure. Therefore, the experimental data of d*a*/d*N*, Δ*K*, and *X* are grouped into three specific intervals: 0–2 mm, 2–6 mm, and 6–15 mm, as shown in Figure 10.

Figure 10a illustrates d*a*/d*N* as a function of Δ*K* within the 0–2 mm depth range from the specimen surface. Based on the data points presented in Figure 10a, the relationship between d*a*/d*N* and Δ*K* follows the Paris Law, which is expressed as:

$$\frac{\mathrm{d}a}{\mathrm{d}N} = C(\Delta K)^m \tag{5}$$

A fitting procedure can be performed to establish the relationship between d*a*/d*N* and Δ*K*, and the parameters *C* and *m* can be obtained as follows:

$$\lg\frac{\mathrm{d}a}{\mathrm{d}N} = -17.65 + 6.50\lg(\Delta K) \tag{6}$$

The corresponding linear correlation coefficient *r* is 0.691, and the standard deviation *δ* is 0.79. Thus, Equation (6) can be rewritten as:

$$\frac{\mathrm{d}a}{\mathrm{d}N} = 2.24\times10^{-18}\Delta K^{6.50} \tag{7}$$

where d*a*/d*N* is in unit of m/cycle, and Δ*K* is in unit of MPa·m$^{1/2}$.

Figure 10b illustrates the variation in d*a*/d*N* with Δ*K* within the 2–6 mm depth range from the specimen surface, which corresponds to the transition layer of the actual axle surface. It can be observed that d*a*/d*N* exhibits significant scatter. To better analyze the data, the results shown in Figure 10b are further divided into two subregions: 2–4 mm (marked in black) and 4–6 mm (marked in red). The data reveal that the region closer to the surface (2–4 mm) exhibits relatively higher fatigue crack growth resistance compared to the deeper region (4–6 mm).

Figure 10c shows d*a*/d*N* versus Δ*K* within the 6–15 mm depth range, corresponding to the core matrix microstructure of the axle. Based on the data points from Figure 10c, a fitting process following the Paris Law yields the relationship as:

$$\lg\frac{\mathrm{d}a}{\mathrm{d}N} = -12.67 + 3.54\lg(\Delta K) \tag{8}$$

The corresponding linear correlation coefficient r is 0.696, and the standard deviation δ is 0.68, which turns Equation (8) into:

$$\frac{\mathrm{d}a}{\mathrm{d}N} = 2.14\times10^{-13}\Delta K^{3.54} \tag{9}$$

where da/dN is in unit of m/cycle, and ΔK is in unit of MPa·m$^{1/2}$.

By comparing Figure 10a with Figure 10b,c, and correspondingly comparing Equation (7) with Equation (9), it is evident that within ΔK of 10–40 MPa·m$^{1/2}$, da/dN in the hardened surface layer of the actual axle is relatively slower than that in the transition layer and the core matrix. This observation indicates that the hardened surface layer of the axle possesses a relatively higher resistance to fatigue crack growth, effectively impeding crack propagation under equivalent stress intensity factor conditions.
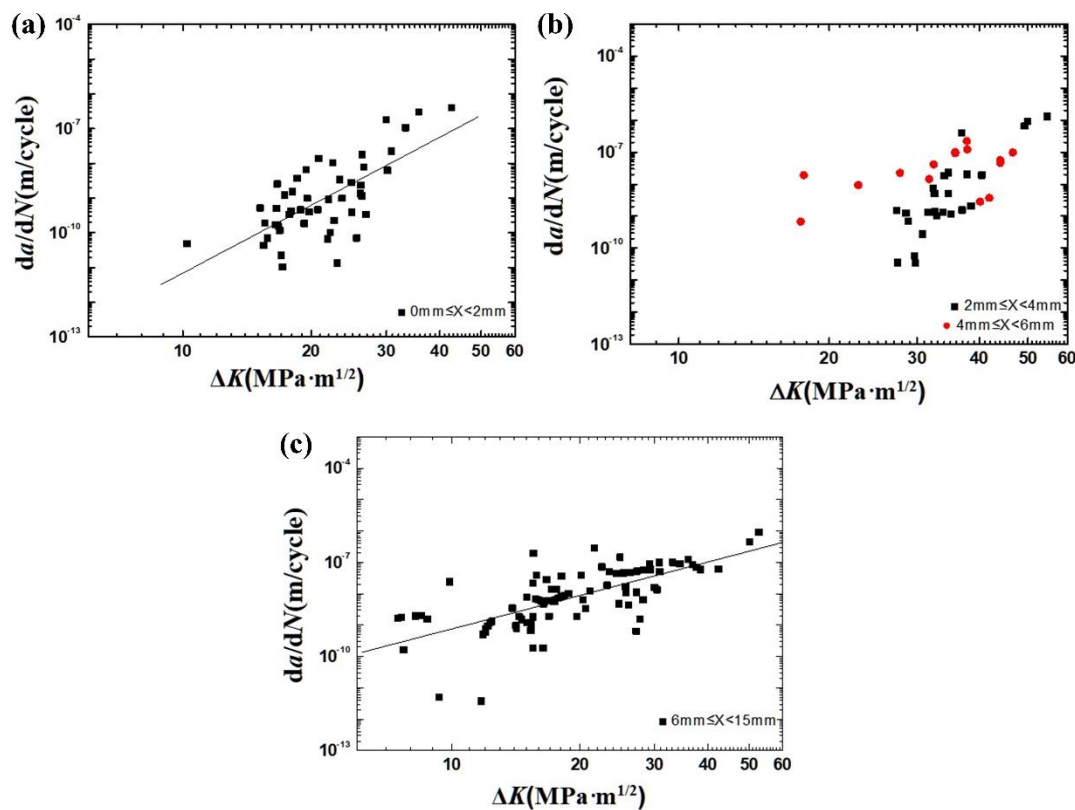

Figure 10. Relationship between *da/dN* and *ΔK* within different depth ranges from the specimen surface: (a) 0–2 mm; (b) 2–6 mm; (c) 6–15 mm.

5. Conclusions

In this paper, an experimental investigation was performed on the fatigue crack growth behavior of an axle steel that contains a hardened surface layer with gradient microstructure. The main conclusions are summarized as follows:

(1) Three-point bending specimens were extracted from the actual S38C axle, with the tensile side representing the hardened surface layer of the axle. Through three-point bending fatigue loading combined with crack length monitoring, the fatigue crack growth characteristics of the axle's surface material, which features a gradient in hardness, were effectively captured. The experimental results reveal the relationship between the fatigue crack growth rate and the stress intensity factor range across three distinct microstructural regions of the axle material: the hardened surface layer (0–2 mm), the transition layer (2–6 mm), and the core matrix (beyond 6

mm). This stratification allows for a comprehensive understanding of how the material's microstructural gradient influences fatigue crack propagation under cyclic loading conditions.

(2) In the hardened surface layer of the axle, within the depth range of 0–2 mm from the surface, the relationship between da/dN and ΔK is represented by the following expression:

$$\frac{\mathrm{d}a}{\mathrm{d}N} = 2.24{\times}10^{-18}\Delta K^{6.50}$$

where da/dN is in unit of m/cycle, and ΔK is in unit of MPa·m$^{1/2}$.

(3) In the core matrix of the axle, specifically within the depth range of 6–15 mm from the surface, the relationship between da/dN and ΔK is represented by the following expression:

$$\frac{\mathrm{d}a}{\mathrm{d}N} = 2.14{\times}10^{-13}\Delta K^{3.54}$$

where da/dN is in unit of m/cycle, and ΔK is in unit of MPa·m$^{1/2}$.

(4) The comprehensive comparison indicates that the hardened surface layer of the axle exhibits significantly higher resistance to fatigue crack growth compared to both the transition layer and the core matrix.

References

1. Glossary: High-speed rail. Available online: https://ec.europa.eu/eurostat/statistics-explained/index.php?title=Glossary:High-speed_rail (accessed on April 6, 2025).

2. High-speed rail. Available online: https://en.wikipedia.org/wiki/High-speed_rail (accessed on April 6, 2025).

3. Ollivier, G.; Bullock, R.; Jin, Y.; Zhou, N. *High-Speed Railways in China: A Look at Traffic*; World bank: Washington, DC, USA, 2014.

4. Zerbst, U.; Klinger, C.; Klingbeil, D. Structural assessment of railway axles - A critical review. *Eng. Fail. Anal.* **2013**, *35*, 54–65.

5. Tong, Y.Y.; Liu, G.X.; Yousefian, K.; Jing, G.Q. Track Vertical Stiffness -Value, Measurement Methods, Effective Parameters and Challenges: A review. *Transp. Geotech.* **2022**, *37*, 100833.

6. Pan, X.; Su, H.; Sun, C.; Hong, Y. The behavior of crack initiation and early growth in high-cycle and very-high-cycle fatigue regimes for a titanium alloy. *Int. J. Fatigue* **2018**, *115*, 67–78.

7. Sun, C.; Song, Q.; Zhou, L.; Pan, X. Characteristic of interior crack initiation and early growth for high cycle and very high cycle fatigue of a martensitic stainless steel. *Mater. Sci. Eng. A* **2019**, *758*, 112–120.

8. Pan, X.; Hong, Y. High-cycle and very-high-cycle fatigue behaviour of a titanium alloy with equiaxed microstructure under different mean stresses. *Fatigue Fract. Eng. Mater. Struct.* **2019**, *42*, 1950–1964.

9. Chang, Y.; Zheng, L.; Pan, X.; Hong, Y. Further investigation on microstructure refinement of internal crack initiation region in VHCF regime of high-strength steels. *Frattura ed Integrità Strutturale* **2019**, *13(49)*, 1-11.

10. Pan, X.; Xu, S.; Qian, G.; Nikitin, A.; Shanyavskiy, A.; Palin-Luc, T.; Hong, Y. The mechanism of internal fatigue-crack initiation and early growth in a titanium alloy with lamellar and equiaxed microstructure. *Mater. Sci. Eng. A* **2020**, *798*, 140110.

11. Chang, Y.; Pan, X.; Zheng, L.; Hong, Y. Microstructure refinement and grain size distribution in crack initiation region of very-high-cycle fatigue regime for high-strength alloys. *Int. J. Fatigue* **2020**, *134*, 105473.

12. Cong, T.; Qian, G.; Zhang, G.; Wu, S.; Pan, X.; Du, L.; Liu, X. Effects of inclusion size and stress ratio on the very-high-cycle fatigue behavior of pearlitic steel. *Int. J. Fatigue* **2021**, *142*, 105958.

13. Pan, X.; Su, H.; Liu, X.; Hong, Y. Multi-scale fatigue failure features of titanium alloys with equiaxed or bimodal microstructures from low-cycle to very-high-cycle loading numbers. *Mater. Sci. Eng. A* **2024**, *890*, 145906.

14. Pan, X.; Xu, S.; Nikitin, A.; Shanyavskiy, A.; Palin-Luc, T.; Hong, Y. Crack initiation induced nanograins and facets of a titanium alloy with lamellar and equiaxed microstructure in very-high-cycle fatigue. *Mater. Lett.* **2024**, *357*, 135769.

15. Weiss, V.; Lal, D.N. Threshold condition for fatigue crack-propagation. *Metall. Trans.* **1974**, *5(8)*, 1946–1949.

16. Schijve, J. *Fatigue of Structures and Materials*, 2nd ed.; Springer: Dordrecht, Germany, 2009.

17. Dowling, N.E. *Mechanical Behavior of Materials: Engineering Methods for Deformation, Fracture, and Fatigue*, 4th ed.; Pearson: Boston, MA, USA, 2013.

18. Chen, Z.; Dai, Y.; Liu, Y. Crack propagation simulation and overload fatigue life prediction via enhanced physics-informed neural networks. *Int. J. Fatigue* **2024**, *186*, 108382.

19. Chen, Z.; Dai, Y.; Liu, Y. Structural fatigue crack propagation simulation and life prediction based on improved XFEM-VCCT. *Eng. Fract. Mech*. **2024**, *310*, 110519.

20. Mourad, A.H.I.; Sajith, S.; Shitole, S.; Almomani, A.; Khan, S.H.; Elsheikh, A.; Alzo'ubi, A.K. Fatigue life and crack growth prediction of metallic structures: A review. *Structures* **2025**, *76*, 109031.

21. Sangid, M.D. The physics of fatigue crack propagation. *Int. J. Fatigue* **2025**, *197*, 108928.

22. Meyers, M.A.; Mishra, A.; Benson, D.J. Mechanical properties of nanocrystalline materials. *Prog. Mater. Sci*. **2006**, *51(4)*, 427–556.

23. Zhang, S.; Xie, J.; Jiang, Q.; Zhang, X.; Sun, C.; Hong, Y. Fatigue crack growth behavior in gradient microstructure of hardened surface layer for an axle steel. *Mater. Sci. Eng. A* **2017**, *700*, 66–74.

24. Lei, Y.B.; Wang, Z.B.; Xu, J.L.; Lu, K. Simultaneous enhancement of stress- and strain-controlled fatigue properties in 316L stainless steel with gradient nanostructure. *Acta Mater*. **2019**, *168*, 133–142.

25. Pan, X.; Qian, G.; Wu, S.; Fu, Y.; Hong, Y. Internal crack characteristics in very-high-cycle fatigue of a gradient structured titanium alloy. *Sci. Rep.* **2020**, *10*, 4742.

26. Garnham, J.E.; Davis, C.L. The role of deformed rail microstructure on rolling contact fatigue initiation. *Wear* **2008**, *265(9–10)*, 1363–1372.

27. Klinger, C.; Bettge, D. Axle fracture of an ICE3 high speed train. *Eng. Fail. Anal*. **2013**, *35*, 66–81.

28. Fu, Z.K.; Ding, H.H.; Wang, W.J.; Liu, Q.Y.; Guo, J.; Zhu, M.H. Investigation on microstructure and wear characteristic of laser cladding Fe-based alloy on wheel/rail materials. *Wear* **2015**, *330*, 592–599.

29. Hassani-Gangaraj, S.M.; Carboni, M.; Guagliano, M. Finite element approach toward an advanced understanding of deep rolling induced residual stresses, and an application to railway axles. *Mater. Design* **2015**, *83*, 689–703.

30. Hu, Y.; Zhou, L.; Ding, H.H.; Lewis, R.; Liu, Q.Y.; Guo, J.; Wang, W.J. Microstructure evolution of railway pearlitic wheel steels under rolling-sliding contact loading. *Tribol. Int*. **2021**, *154*, 106685.

31. Unal, O.; Maleki, E.; Karademir, I.; Husem, F.; Efe, Y.; Das, T. Effects of conventional shot peening, severe shot peening, re-shot peening and precised grinding operations on fatigue performance of AISI 1050 railway axle steel. *Int. J. Fatigue* **2022**, *155*, 106613.

32. Du, S.; Wang, K.; Hu F. Overview and prospect of axle technology for high speed trains at home and abroad. *Mater. China* **2019**, *38(7)*, 641–650. (in Chinese)

33. Liu, L.; Ma, Y.; Liu, S.; Wang, S. The fatigue behaviors of a medium-carbon pearlitic wheel-steel with elongated sulfides in high-cycle and very-high-cycle regimes. *Materials* **2021**, *14(15)*, 4318.

34. Klenam, D.E.P.; Chown, L.H.; Papo, M.J.; Cornish, L.A. Steels for rail axles-an overview. *Crit. Rev. Solid State Mater. Sci*. **2024**, *49(2)*, 163–193

35. Zhang, R.; Zheng, C.; Lv, B.; Wang, X.; Li, X.; Li, Y.; Zhang, F. Research progress on rolling contact fatigue damage of bainitic rail steel. *Eng. Fail. Anal*. **2023**, *143*, 106875.

36. Lewis, R.; Olofsson, U. Mapping rail wear regimes and transitions. *Wear* **2004**, *257(7–8)*, 721–729.

37. Enblom, R.; Berg, M. Simulation of railway wheel profile development due to wear - influence of disc braking and contact environment. *Wear* **2005**, *258(7–8)*, 1055–1063.

38. Braghin, F.; Lewis, R.; Dwyer-Joyce, R.S.; Bruni, S. A mathematical model to predict railway wheel profile evolution due to wear. *Wear* **2006**, *261(11–12)*, 1253–1264.

39. Hirakawa, K.; Toyama, K.; Kubota, M. The analysis and prevention of failure in railway axles. *Int. J. Fatigue* **1998**, *20(2)*, 135–144.

40. Ekberg, A; Kabo, E. Fatigue of railway wheels and rails under rolling contact and thermal loading - an overview. *Wear* **2005**, *258(7–8)*, 1288–1300.

41. Zerbst, U.; Mädler, B.; Hintze, H. Fracture mechanics in railway applications: an overview. *Eng. Fract. Mech.* **2005**, *72(2)*, 163–194.

42. Zerbst, U.; Beretta, S.; Köhler, G.; Lawton, A.; Vormwald, M.; Beier, H.T.; Klinger, C.; Cerny, I.; Rudlin, J.; Heckel, T.; Klingbeil, D. Safe life and damage tolerance aspects of railway axles - A review. *Eng. Fract. Mech.* **2013**, *98*, 214–271.

43. Ekberg, A; Åkesson, B; Kabo, E. Wheel/rail rolling contact fatigue - Probe, predict, prevent. *Wear* **2014**, *314(1–2)*, 2–12.

44. Murakami, Y. Metal Fatigue: Effect of Small Defects and Nonmetallic Inclusions; Elsevier: Oxford, UK, 2002.

45. Pan, X.; Du, L.; Qian, G.; Hong, Y. Microstructure features induced by fatigue crack initiation up to very-high-cycle regime for an additively manufactured aluminium alloy. *J. Mater. Sci. Technol.* **2024**, *173*, 247–260.

46. Pan, X.; Hong, Y. High-cycle and very-high-cycle fatigue of an additively manufactured aluminium alloy under axial cycling at ultrasonic and conventional frequencies. *Int. J. Fatigue* **2024**, *185*, 108363.

47. Du, L.; Pan, X.; Hong, Y. New insights into microstructure refinement in crack initiation region of very-high-cycle fatigue for SLM Ti-6Al-4V via precession electron diffraction. *Materialia* **2024**, *33*, 102008.

48. Pan, X.; Qian, G.; Hong, Y. Nanograin formation in dimple ridges due to local severe-plastic-deformation during ductile fracture. *Scr. Mater.* **2021**, *194*, 11363.

49. Du, L.; Pan, X.; Qian, G.; Zheng, L.; Hong, Y. Crack initiation mechanisms under two stress ratios up to very-high-cycle fatigue regime for a selective laser melted Ti-6Al-4V. *Int. J. Fatigue* **2021**, *149*, 106294.

50. Yap, C.Y.; Chua, C.K.; Dong, Z.L.; Liu, Z.H.; Zhang, D.Q.; Loh, L.E.; Sing, S.L. Review of selective laser melting: Materials and applications. *Appl. Phys. Rev.* **2015**, *2*, 041101.

51. DebRoy, T.; Wei, H.L.; Zuback, J.S.; Mukherjee, T.; Elmer, J.W.; Milewski, J.O.; Beese, A.M.; Wilson-Heid, A.; De, A.; Zhang, W. Additive manufacturing of metallic components—Process, structure and properties. *Prog. Mater. Sci.* **2018**, *92*, 112–224.

52. Qian, G.; Jian, Z.; Pan, X.; Berto, F. In-situ investigation on fatigue behaviors of Ti-6Al-4V manufactured by selective laser melting. *Int. J. Fatigue* **2020**, *133*, 105424.

53. Qian, G.; Jian, Z.; Qian, Y.; Pan, X.; Ma, X.; Hong, Y. Very-high-cycle fatigue behavior of AlSi10Mg manufactured by selective laser melting: Effect of build orientation and mean stress. *Int. J. Fatigue* **2020**, *138*, 105696.

54. Badoniya, P.; Srivastava, M.; Jain, P.K.; Rathee, S. A state-of-the-art review on metal additive manufacturing: Milestones, trends, challenges and perspectives. *J. Braz. Soc. Mech. Sci.* **2024**, *46*, 339.

55. Tao, Z.; Wang, Z.; Pan, X.; Su, T.; Long, X.; Liu, B.; Tang, Q.; Ren, X.; Sun, C.; Qian, G.; et al. A new probabilistic control volume scheme to interpret specimen size effect on fatigue life of additively manufactured titanium alloys, *Int. J. Fatigue* **2024**, *183*, 108262.

56. Xu, S.; Pan, S.; Li, Z.; Li, S.; He, X.; Pan, X. Anisotropic tensile behavior and fracture characteristics of an additively manufactured nickel alloy without and with a heat treatment of solution aging. *Mater. Sci. Eng. A* **2025**, *927*, 148015.

57. Tan, X.; Kok, Y.; Tan, Y.J.; Descoins, M.; Mangelinck, D.; Tor, S.B.; Leong, K.F.; Chua, C.K. Graded microstructure and mechanical properties of additive manufactured Ti-6Al-4V via electron beam melting. *Acta Mater.* **2015**, *97*, 1–16.

58. Long, X.; Jia, Q.; Li, J.; Chong, K.; Du, L.; Pan, X.; Chang, C. Mechanical properties and parameter optimization of TC4 alloy by additive manufacturing. *China Surf. Eng.* **2022**, *35*, 215–223. (in Chinese)

59. Gao, C.; Zhang, Y.; Jiang, J.; Fu, R.; Du, L.; Pan, X. Research viewpoint on performance enhancement for very-high-cycle fatigue of Ti-6Al-4V alloys via laser-based powder bed fusion. *Crystals* **2024**, *14(9)*, 749.

60. Xu, W.; Lui, E.W.; Pateras, A.; Qian, M.; Brandt, M. In situ tailoring microstructure in additively manufactured Ti-6Al-4V for superior mechanical performance. *Acta Mater.* **2017**, *125*, 390–400.

Disclaimer/Publisher's Note: The statements, opinions and data contained in all publications are solely those of the individual author(s) and contributor(s) and not of MDPI and/or the editor(s). MDPI and/or the editor(s) disclaim responsibility for any injury to people or property resulting from any ideas, methods, instructions or products referred to in the content.